A Systematic Material Characterization Method via Near-field Scanning Microwave Microscopy

Yulong Zhou, Ning Leng, Zhun Wei, *Member, IEEE*, Xiuzhu Ye, *Senior Member, IEEE*, Ming Bai, and Xudong Chen, *Fellow, IEEE*

***Abstract*—Accurate measurement of material dielectric property is essential for engineers to synthesize microwave devices. This paper proposes a systematic material characterization method via the coaxial resonator (CR) based near-field scanning microwave microscopy (NFSMM) with an arbitrary tip shape, from the modelling method to the inversion algorithm. The effective interaction region in the CR-based NFSMM is investigated and determined, which contributes most to the contrast capacitance caused by the tip-sample interaction. Then the Huygens' principle is applied in the forward solver of NFSMM when the samples under test are homogeneous. The relative error of our model is less than 2.1% in numerical validations. Based on the proposed forward solver, a dielectric characterization method via the conjugate gradient algorithm is proposed and verified with experimental results. The retrieved permittivity of unknown samples matches well with that measured by the transmission line method, and the discrepancy between the two results is less than 3%. The proposed systematic method is promising to provide a new pathway to quantitatively determine the dielectric property of homogeneous samples.**

***Index Terms*—dielectric characterization, Huygens' principle, nonlinear inversion, coaxial resonator, near-field scanning microwave microscopy (NFSMM)**

I. Introduction

Dielectric properties of materials are essential for researchers and engineers to analyze and synthesize microwave devices. Therefore, a simple and accurate measurement method is very important in both academic and industrial aspects. Traditional methods of determining these properties include transmission line techniques, split cavity techniques, free space techniques, etc [1]–[6]. While these traditional methods have their own advantages, they also present some drawbacks in certain aspects. Transmission line techniques requires the material to be fitted into the cross-section of waveguide. Split cavity techniques require the dimension of the investigated sample to be larger than the diameter of the cylinder waveguide. Free space techniques require the sample size to be large enough to avoid the inaccuracy caused by the diffraction at the edge.

With the advent of the near-field scanning microwave microscopy (NFSMM), a new nondestructive method could be used in characterizing the dielectric property of samples, which does not reqiure a well-defined geometric form of samples [7]–[9]. With the aid of the calibration technique, the measurement accuracy of the NFSMM is improved, which paves the way for quantitative characterization [10], [11]. Various designs of NFSMMs are demonstrated, such as scanning tunneling microscopy [12]–[14], atomic-force microscopy (AFM) based NFSMM [15]–[20], coaxial resonantor (CR) based NFSMM [21]–[24], etc. Due to the tunnel effect on the surface of the conductive material, the scanning tunneling microscopy could record the tunnel current to maintain the tip-sample distance, which could provide a topograghic image during the material characterization [12]–[14]. The AFM-based NFSMM could achieve a high-resolution image on dielectric properties of the sample, together with the topography information of the sample. Due to the sharpness of the tip and the feedback control system, microscale even nanoscale resolution could be realized [15]–[20]. However, some samples used in microwave device design are at milli-scale or centi-scale, and the property determination of these samples via AFM-based NFSMM will be time-consuming and in additional costly. To characterize the dielectric property of these samples, the CR-based NFSMM seems to be a good choice due to its easy fabrication and implementation, as well as low cost [21]–[24]. Due to lack of the tip-sample distance control system, it performs better in the sample with flat surface. In modelling procedure, the accuracy of the result mainly depends on the model's ability to solve the tip-sample interaction problems. Among existing modelling methods, the tip shape is usually replaced by a conducting sphere or a unit dipole, which nevertheless could bring the inaccuracy to the tip-sample interaction solution [22], [25], [26]. The modelling method of the arbitrary tip shape in the CR-based NFSMM is rarely reported.

In this paper, a systematic material characterization method, from the modelling method to the inversion algorithm, via the CR-based NFSMM is proposed. In simulation, the proposed truncated model could be applied to an arbitrary tip shape. The region beneath the tip is determined and referred to as the effective interaction region, which contributes most to the contrast capacitance caused by the tip-sample interaction. Based on the determined effective region, the Huygens' principle is then applied in the forward solver of NFSMM when

Manuscript received January 23, 2022; revised March 04, 2022; accepted March 14, 2022. This work was supported in part by the Singapore Ministry of Education grant under Project No. MOE2019-T2-1-117, in part by the National Natural Science Foundation of China (NSFC) under Grants 61971036, in part by Fund of Key Laboratory for Information Science of Electromagnetic Waves (MoE) under Grant EMW201903, and in part by Beijing Institute of Technology Research Fund Program for Young Scholars. The first two authors contributed equally to this work. Xudong Chen indicates corresponding author.

Y. Zhou and X. Chen are with the Department of Electrical and Computer Engineering, National University of Singapore, 117583 Singapore (e-mail: e0338289@u.nus.edu; elechenx@nus.edu.sg).

N. Leng and M. Bai are with the Beihang University, Beijing, 100191, China. (e-mail: lengningy@buaa.edu.cn; mbai@buaa.edu.cn).

Z. Wei is with College of Information Science and Electronic Engineering, Zhejiang University, Hangzhou, China. (e-mail: eleweiz@zju.edu.cn).

X. Ye is with the Beijing Institute of Technology, Beijing 100811, China. (e-mail: xiuzhuye@outlook.com).

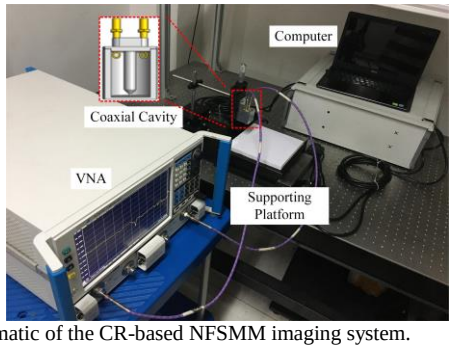

Fig. 1 Schematic of the CR-based NFSMM imaging system.

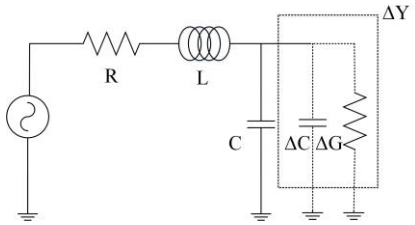

Fig. 2. Typical equivalent circuit of NFSMM.

investigating homogeneous samples. The relative error of the proposed model is less than 2.1% in many simulations, which proves the validity of the proposed forward solver. Based on the proposed forward solver, a dielectric characterization method via the conjugate gradient algorithm is proposed for dielectric characterization. To validate the proposed characterization method, two unknown thick homogeneous samples are tested. The retrieved permittivity matches well with that measured by the transmission line method, and the discrepancy between the two results is less than 3%.

The main contributions of this paper are listed as follows. Firstly, a truncated model is proposed for investigating the tip-sample interaction in the CR-based NFSMM. We introduce valid boundary conditions at the truncation surfaces to ensure the accuracy of the proposed truncation model. Since the computational domain is reduced, the computation cost is significantly reduced. Secondly, we find that the electric energy of a thick sample (usually more than 4 mm) mainly concentrates in a small region beneath the tip. Due to the specific structure of the CR-based cavity, the contrast capacitance is more sensitive to the tip-sample distance rather than the thickness of the investigated sample, which could simplify the measurement procedure for the dielectric characterization of the sample. Thirdly, a forward solver based on the Huygens' principle is proposed for the CR-based NFSMM with an arbitrary tip shape when investigating homogeneous samples, which could reduce the computational cost in the forward formulation since only a surface integral is involved. Finally, an iterative algorithm is proposed to characterize dielectric properties of the investigated sample based on the proposed forward solver, which can be used to characterize samples without resorting to the time-consuming process of building up a database by doing a lot of experiments or computations for various samples.

The paper is structured as follows. Section II presents the fundamental principle, which includes the relationship between the variation of S_{11} and the change in the tip-sample interaction, the commercial-software simulation model of the tip-sample interaction, and the effective region investigation. Section III proposes the application of the Huygens' principle in the forward solver of NFSMM and its numerical validation. The inverse formulation to characterize the sample permittivity is given in Section IV. An experimental validation is demonstrated to verify the performance of the proposed method. The conclusion is made in section V.

II. Simulation Modelling

As illustrated in Fig. 1, the measurement setup of the CR-based NFSMM consists of four parts: the vector network analyzer (VNA), the coaxial cavity with a sharp tip, the x-y 2D motor stage and the computer. In the measurement, the input signal of the coaxial cavity is generated by the VNA and transmitted via the coaxial cable. The reflected signal can be detected and monitored by the VNA. The x-y 2D motor stage supports the sample and is controlled by the computer, the precision of which is 1 μm. The movement of the coaxial resonator along the z can be controlled with the step size of 20 μm. The variation of S_{11} is recorded in the VNA for data post-processing.

The equivalent circuit of the CR-based NFSMM is demonstrated in Fig. 2. According to the equivalent circuit, any changes in the tip-sample interaction of the CR-based NFSMM will perturb the value of the admittance, leading to a variation of S_{11} at a certain frequency in the VNA. Therefore, the S_{11} can be expressed as a function of the admittance Y [27]–[29]:

$$S_{11} = f(Y) \tag{1}$$

If the admittance Y is due to a small perturbation around a reference admittance Y_0, which is the admittance between tip and sample in absence of perturbation with respect to a certain chosen background medium, then the Taylor expansion yields,

$$S_{11}(Y) = S_{11}(Y_0) + S'_{11}(Y_0)(Y - Y_0) + \ldots. \tag{2}$$

Since the contrast admittance ΔY, defined as $Y - Y_0$, is small, the higher orders of the contrast admittance in (2) can be ignored. The relationship between the variation of S_{11} and the contrast admittance can be well approximated as:

$$\Delta S_{11} \approx S'_{11}(Y_0)\Delta Y\,. \tag{3}$$

where ΔS_{11} is the variation of S_{11} due to the perturbation in the reference sample and is calculated as $S_{11}(Y) - S_{11}(Y_0)$ at the certain frequency. In this case, the S'_{11} can be obtained via the calibration on the reference sample, and then the obtained value S'_{11} can be used to directly convert the measured ΔS_{11} to the contrast admittance, which depends on the physical properties of samples under test. Essentially, (3) is the fundamental principle of NFSMM that establishes the relationship between the measured signal ΔS_{11} and the sample's property ΔY. Both the forward problem and the inverse problem discussed in this paper are in principle governed by (3). After obtaining the contrast admittance ΔY, the contrast conductance ΔG and contrast capacitance ΔC can be calculated as

$$\Delta Y = \Delta G + j\omega\Delta C\,. \tag{4}$$

A. *Commercial-software Simulation Model Setup*

As shown in Fig. 3(a), a simulation model with full CR-

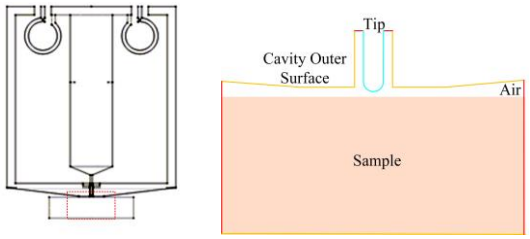

Fig. 3. Simulation model of the CR-based NFSMM imaging system. (a) Full structure model (b) Truncated model.

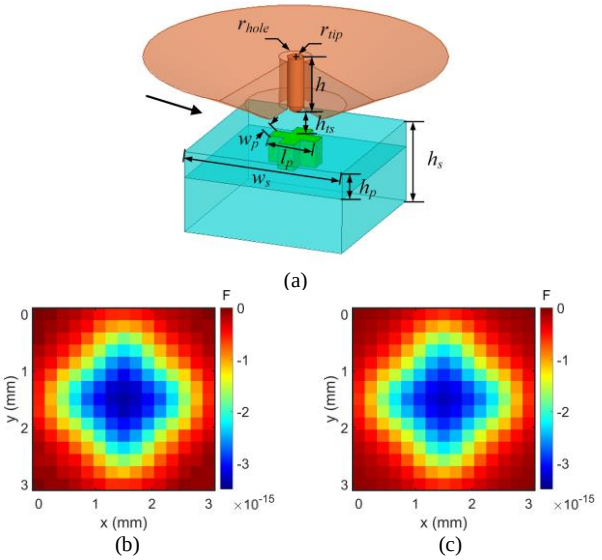

Fig. 4. A 3D sample for scanning procedure. (a) A cross-shape perturbation. Simulated C_{contrast} image via (b) full structure model and (c) truncated model. Parameters used in the calculation: r_{hole} = 0.8 mm, h = 3.51 mm, r_{tip} = 0.4 mm, h_{ts} = 0.2 mm, h_s = 5 mm, w_s = 12.5 mm, h_p = 1.6 mm, l_p = 2.4 mm, w_p = 0.8 mm (Not to scale).

based NFSMM structure is set up. The computational cost in the simulation is large due to the large dimension of the full structure. In [30], the direction of the electric field in the bottom hole of the CR-based NFSMM is along the radial direction when the working frequency is at its first resonance. The electric field distribution inside the CR-based NFSMM motivates us to propose the truncated model shown in Fig. 3(b), which is the region inside the red dotted line in Fig. 3(a). The operating frequency of the NFSMM in our work is 1.41 GHz, at which the resonant mode is TEM mode. Since the size of the tip and the tip-sample distance are smaller than one percent wavelength at the operating frequency, the quasi-static regime is considered in the simulation. In the truncated model, we set the surface of the tip as the terminal (blue line), the bottom surface of the sample and the outer surface of the cavity hole as the ground (i.e., zero potential) that is labelled in yellow, and the top and side boundaries as the zero-charge (i.e., the electric flux perpendicular to the surface is zeros) that is labelled in red. Since the computation domain is large enough, the normal of the electric field on the side boundary is weak and can be neglected. In this way, the side boundary is set as the zero-charge. The truncated domain, together with the above-mentioned boundary conditions, suffices to well approximate the tip-sample interaction. For instance, a cross-shape perturbation (1.6 mm, ε_r = 1) is added into the Quartz sample

TABLE I
COMPARISON OF THE COMPUTATION COST FOR A SINGLE POINT

	Full Structure Model	Truncated Model
Required Memory	23.93 GB	11.15 GB
Computation Time	433 s	12 s

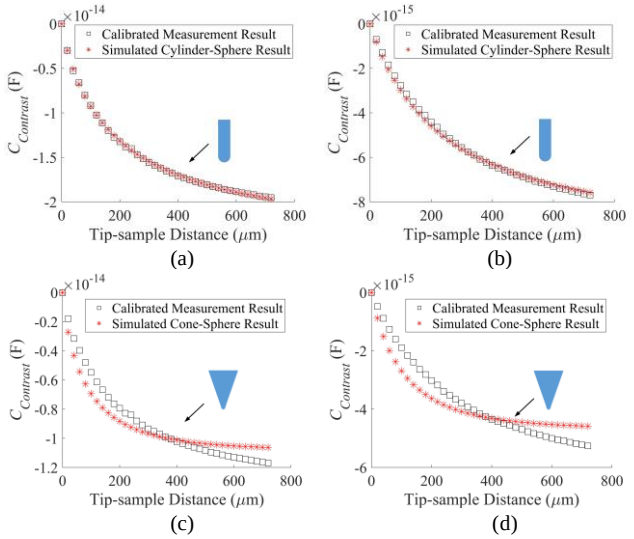

Fig. 5. The comparison between the calibrated measurement result and the simulation result. Comparison of the cylinder-sphere tip for (a) 2 mm Quartz and (b) 5 mm FR4. Comparison of the cone-sphere tip for (c) 2 mm Quartz and (d) 5 mm FR4.

(5 mm, ε_r = 3.8) and scanned with the step size of 0.2 mm, as shown in Fig. 4. In simulation, the capacitance without the perturbation is chosen as the reference capacitance, and the capacitance at different scanning points are recorded. As a result, the change in the capacitance, referred to as the contrast capacitance C_{contrast}, can be obtained. There is only a small visual difference between the truncated model result (denoted as $\bar{A}$) and the full structure model result (denoted as $\bar{B}$) and the relative error between is only 4.10%, where the relative error is defined as $\|\bar{A}-\bar{B}\|_2 / \|\bar{B}\|_2$. Moreover, the time consumption of the proposed truncated model is smaller due to the smaller computational domain, which is summarized in Table I. The truncated model could significantly reduce the computational time of the AC/DC module in COMSOL.

In order to verify the accuracy of the proposed truncated model, a calibration procedure is implemented. In measurement, the cylinder-sphere tip and two homogeneous samples with different permittivity and thickness are used. One is the Quartz sample (2 mm, ε_r = 3.8), the other one is the FR4 sample (5 mm, ε_r = 2). The resonant frequency 1.41 GHz in the contact mode is selected as the reference frequency, at which the variation of S_{11} is recorded with the increasing tip-sample distance. In simulation, the capacitance in the contact mode is chosen as the reference capacitance, and the contrast capacitance C_{contrast} at different tip-sample distances can be obtained. Then the $S'_{11}(Y_0)$ can be calculated via the least square method, according to the definition in (3). The simulation results of the truncated model with a cylinder-sphere tip are demonstrated in Fig. 5(a) and (b). There is a small discrepancy between the simulated C_{contrast} (denoted as $\bar{A}$) and

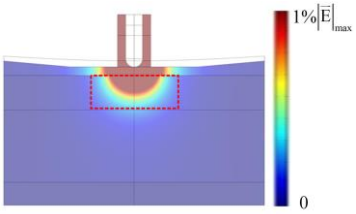

Fig. 6. The distribution of the electric field in the whole computation space. For a better visual effect, magnitudes that are higher than 1% of the maximum value of electric field are shown as the same color (red).

the calibrated measurement result (denoted as $\bar{B}$). The relative error R_e (calculated as $\|\bar{A} - \bar{B}\|_2 / \|\bar{B}\|_2$) is 0.58% in 2 mm Quartz calibration and 2.07% in 5 mm FR4 calibration. Moreover, to show that a more accurate simulation result is obtained by using a tip shape that better matches the physical experimental NFSMM tip, we have conducted simulations for a cone-sphere tip and presented the simulation results in Fig. 5(c) and (d). Note that the tip used in the experiment is cylinder-sphere, as shown in Fig. 5(a) and (b), where we see that the simulations results match well with the measurement results. The poor match in Fig. 5(c) and (d) is obviously due to the discrepancy in tip shapes used in simulation and experiment.

B. *Determination of Effective Interaction Region*

For the AFM-based NFSMM, the contribution of contrast capacitance in tip-sample interaction comes primarily from the perturbation of a limited window (effective interaction region) beneath the tip [31]. For the CR-based NFSMM, it is also important to investigate the effective interaction region. The determination of the effective interaction region not only reduces the computation domain of the tip-sample interaction, but also creates the condition for the application of Huygens' principle in the forward solver formulation.

As shown in Fig. 6, the 5.1 mm Quartz (ε_r = 3.8) is selected as the reference sample and the tip-sample distance is set as 0.2 mm in the simulation, which is the defaulted reference condition in this section and later unless otherwise specified. The magnitude of $|\vec{E}|$ in the small region (inside the red dash box) beneath the tip is larger than that away from the tip, which indicates that most energy is concentrated in this small region. This observation motivates us to do various numerical simulations, and we empirically find the contrast capacitance is insensitive to the thickness of the sample once the thickness of the sample is larger than 4 mm. To verify our conclusion, we investigate samples with three different thicknesses, i.e., 4.1 mm, 5.1 mm, and 6.1 mm, and the tip-sample distance is fixed at 0.2 mm. We compare the results obtained by numerically choosing two kinds of reference conditions. First, the reference condition is chosen as when the thickness of reference Quartz samples are consistent with the investigated samples. As illustrated in Fig. 7(a), there are negligible discrepancies among the contrast capacitance at three different thickness with the increasing relative permittivity. Secondly, the thickness of the reference Quartz sample is numerically chosen as a fixed value of 5.1 mm, although this is not physical for the cases of 4.1 mm and 6.1 mm thick samples. Compared with the value at

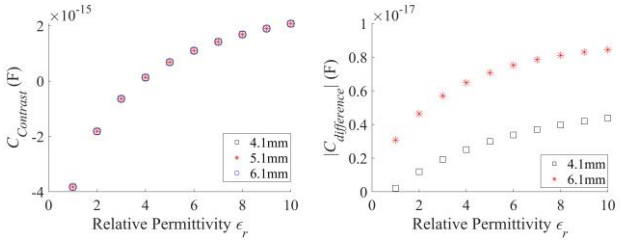

(a) (b)

Fig. 7. The influence of the sample thickness. Samples of three thicknesses are physically tested, for which two different reference conditions are chosen to calculate the contrast capacitance. (a) Contrast capacitance in respect to the ground-truth reference sample with variable thicknesses. (b) Absolute contrast capacitance discrepancy in respect to a mathematical reference sample with the fixed thickness of 5.1 mm.

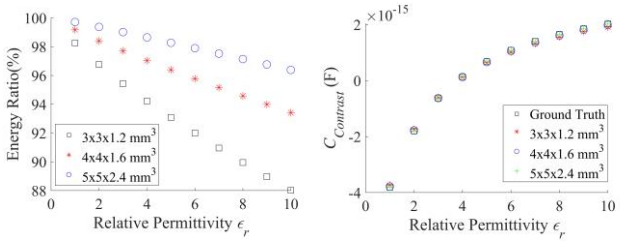

(a) (b)

Fig. 8. The influence of the size of the effective interaction region on (a) Energy ratio and (b) Contrast capacitance.

5.1 mm, the absolute discrepancy among the contrast capacitance at different thicknesses is still small with the increasing relative permittivity, as shown in the Fig. 7(b). These results practically benefit us by simplifying the measurement procedure since the accurate measurement of sample's thickness is relaxed for thick samples.

Since most energy is concentrated in the small region, referred to as the effective interaction region, beneath the tip, sample materials that are outside of this region barely contribute to the measured signal. This is an important observation since we can numerically choose the outside region as another material, without noticeably perturbing the ground truth. The key is to determine the size of effective interaction region. For this purpose, three different sizes of the effective interaction region are selected and compared in Fig. 8. When investigating a homogenous sample with relative permittivity ε_r, we numerically set the sample just inside the effective region as the sample and change the sample outside the effective region to be the reference material, i.e., Quartz. As shown in Fig. 8(a), when the region size is selected as 4×4×1.6 mm^3, the energy in this region is still larger than 93% of the total energy in the whole sample area even the relative permittivity of the sample in the effective region is up to 10. Moreover, the contrast capacitance is also investigated and illustrated in Fig. 8(b), in which the reference capacitance is the capacitance caused by the Quartz sample. We see that the contrast capacitances caused by the three sizes of effective regions are very close to the case of the ground-truth sample. When the effective region is selected as 4×4×1.6 mm^3, the contrast capacitance discrepancy is less than 1.6%. To balance computational load and the accuracy, the effective region is chosen as 4×4×1.6 mm^3.

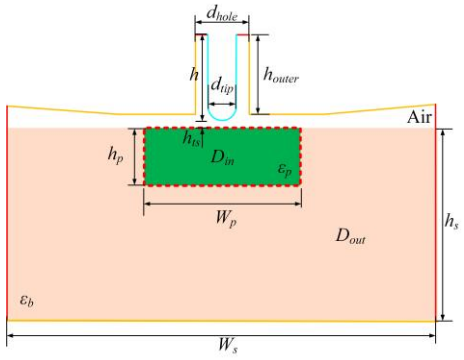

Fig. 9. A typical NFSMM scheme. Parameters used in the calculation: h_{outer} = 3.5 mm, d_{hole} = 1.6 mm, h = 3.51 mm, d_{tip} = 0.8 mm, h_{ts} = 0.2 mm, h_s = 5.1 mm, W_s = 12.5 mm, h_p = 1.6 mm, W_p = 4.6 mm, ε_b = 3.8 (Not to scale). The red dash line denotes the boundary of effective interaction region.

III. Forward Solver in NFSMM

The determination of the effective region reduces the computation domain of the tip-sample interaction to a small block region, which creates a condition to propose a new forward solver of CR-NFSMM. When investigating a new homogeneous sample, we could set the sample just inside the effective region as the new homogeneous sample and change the sample outside the effective region to be the reference sample. As shown in Fig. 9, the background material is homogeneous with the permittivity ε_b. When we study a new homogeneous material with permittivity ε_p, it suffices to change the material only inside the effective region to be a new one with permittivity ε_p, which is referred to as a perturbation with respect to the background material. In this way, the new homogeneous sample inside the effective region could be considered as a small perturbation in the reference sample. Since the sample inside the effective region is homogeneous, the Huygens' principle could be used in the proposed forward solver to calculate the change in capacitance caused by the perturbation [32], [33]. Compared with the method in [29], the computational cost reduces a lot, since only the potential on the surface of the effective region needs to be calculated.

The geometry and parameters used in the calculation are sketched in Fig. 9, and a cylinder-sphere tip is selected and depicted by the height of the whole tip h and the diameter of the tip d_{tip}. A three-dimensional sample is used, which is a cubic region with height h_s and width W_s. The domain inside the effective interaction region denoted as D_{in}, which is depicted by the height h_p and width W_p. The domain outside the effective interaction region denoted as D_{out}. The DC voltage bias between the tip and the ground is set as 1 V.

A. *Theoretical Principle*

The task of the forward solver is to calculate the change in capacitance, referred to as contrast capacitance C_{contrast}, when a perturbation is present. In the domain D_{in}, the potential ϕ satisfies the following equation:

$$\nabla\cdot(\varepsilon(r)\nabla\phi(r))=0\,. \tag{5}$$

In the domain D_{out}, the potential ϕ still satisfies (5), however subject to boundary conditions specified in Section II. A.

According to the Huygens' principle, if the observation point is in the domain D_{in}, the material in the domain D_{out} could be changed to be the perturbation material with the relative permittivity ε_p, then we can get (6) by using Green's Theorem [34]:

$$\phi_1(r)=\oint_{S_0}[-G_p(r,r')\varepsilon_p(r')\frac{\partial\phi_1(r')}{\partial n'}+\phi_1(r')\varepsilon_p(r')\frac{\partial G_p(r,r')}{\partial n'}]da',\ r\in D_{in} \tag{6}$$

where n' is the inward normal direction of the domain D_{in}, and S_0 is the boundary of the domain D_{in}. The subscript 1 denotes the situation that the observation point is in the domain D_{in}. The corresponding Green's function $G_p(r,r')$ is analytically given as:

$$G_p(r,r')=\frac{1}{4\pi\varepsilon_p|r-r'|}. \tag{7}$$

If the observation point is in the domain D_{out}, the material inside the domain D_{in} is changed to be the background medium with the relative permittivity ε_b, and consequently we can arrive at:

$$\phi_2(r)=\phi_2^i(r)+\oint_{S_0}[G_b(r,r')\varepsilon_b(r')\frac{\partial\phi_2(r')}{\partial n'}-\phi_2(r')\varepsilon_b(r')\frac{\partial G_b(r,r')}{\partial n'}]da',\ r\in D_{out} \tag{8}$$

where $G_b(r,r')$ and $\partial G_b(r,r')/\partial n'$, the corresponding background Green's function and its normal-direction derivative on the boundary, can be obtained from the commercial software simulation. These two items account for point (r') to point (r) electrostatic interaction for the working background that includes the tip, air gap, sample, substrate, and ground. In (8), $\phi_2^i(r)$ refers to the background potential in the absence of the perturbation, and the subscript 2 denotes the situation that the observation point is in the domain D_{out}. When observation points in (6) and (8) are infinitely close to the boundary S_0, the following boundary conditions could be applied:

$$\phi_1(r)=\phi_2(r),\ \ r\in S_0 \tag{9}$$

$$\varepsilon_p(r)\frac{\partial\phi_1(r)}{\partial n'}=\varepsilon_b(r)\frac{\partial\phi_2(r)}{\partial n'},\ \ r\in S_0\,. \tag{10}$$

Thus, a linear equation system can be obtained and straightforwardly solved:

$$\phi_2(r)=\oint_{S_0}[-G_p(r,r')\varepsilon_b(r')\frac{\partial\phi_2(r')}{\partial n'}+\phi_2(r')\varepsilon_p(r')\frac{\partial G_p(r,r')}{\partial n'}]da' \tag{11}$$

$$\phi_2(r)=\phi_2^i(r)+\oint_{S_0}[G_b(r,r')\varepsilon_b(r')\frac{\partial\phi_2(r')}{\partial n'}-\phi_2(r')\varepsilon_b(r')\frac{\partial G_b(r,r')}{\partial n'}]da' \tag{12}$$

In discretization procedure on the boundary S_0, the linear interpolation functions are selected as the basis function, and the delta function is chosen as the testing function. For ease of writing, the potential derivative on the boundary is defined as $\bar{q}_2$ ($\bar{q}_2=-\partial\bar{\phi}_2/\partial n'$). The matrix form of (11) and (12) are obtained:

$$\bar{\bar{\mathrm{D}}}\bar{\phi}_2-\bar{\bar{\mathrm{G}}}_p\bar{q}_2=0 \tag{13}$$

$$\bar{\bar{\mathrm{H}}}\bar{\phi}_2-\bar{\bar{\mathrm{G}}}_b\bar{q}_2=\bar{\phi}_2^i \tag{14}$$

where $\bar{\bar{\mathrm{D}}}$, $\bar{\bar{\mathrm{G}}}_p$, $\bar{\bar{\mathrm{H}}}$ and $\bar{\bar{\mathrm{G}}}_b$ are calculated as surface integrals over the boundary element of the D_{in} and their close-form

expressions can be derived.

According to (8), the contrast capacitance C_{contrast} caused by the perturbation in D_{in} can be expressed as the total perturbation electric charge accumulated at the tip boundary,

$$C_{\text{Contrast}} = \oint_{s_0} [G_c(r')\varepsilon_b(r')\frac{\partial \phi_2(r')}{\partial n'} - \phi_2(r')\varepsilon_b(r')\frac{\partial G_c(r')}{\partial n'}]da' \quad (15)$$

where

$$G_c(r') = \oint_{s_{tip}} \varepsilon_0(r)\frac{\partial G_b(r,r')}{\partial N}da. \quad (16)$$

N is defined as the inward normal direction of the tip surface S_{tip}. After discretization, the contrast capacitance is given as:

$$C_{\text{contrast}} = -\bar{L}^T\bar{\phi}_2 - \bar{P}^T\bar{q}_2 \quad (17)$$

where $\bar{L}^T$ and $\bar{P}^T$ are calculated as surface integrals of $\partial G_c(r')/\partial n'$ and $G_c(r')$ over the boundary element of the domain D_{in}. The similar derivation procedure is amply described in the appendix of [29].

For the perturbation with lossy material, the $\varepsilon(r)$ in (5) is changed to a complex value $\varepsilon(r) - j\sigma(r)/\omega$, where $\sigma(r)$ is the conductivity of the lossy sample. Then the ε_p in (6) and ε_b in (8) are complex-valued. The current consists of two types, one due to capacitance and the other due to conductance. The relationship between the charge on the tip and the voltage is

$$Q(\omega) = \frac{I(\omega)}{j\omega} = V(\omega)\left(\frac{G_{ts}(\omega)}{j\omega} + C(\omega)\right). \quad (18)$$

where $G_{ts}(\omega)$ is the conductance between the probe and sample. Under a tip–sample bias of 1 V, the capacitance is equal to the real part of $Q(\omega)$ and, combined with (17), we have

$$C_{\text{contrast}}(\omega) = \text{Re}\left(-\bar{L}^T\bar{\phi}_2 - \bar{P}^T\bar{q}_2\right). \quad (19)$$

Similarly, the contrast conductance is equal to the imaginary part of $Q(\omega)$ and, combined with (17), we have

$$G_{\text{contrast}}(\omega) = \text{Im}\left[\left(\bar{L}^T\bar{\phi}_2 + \bar{P}^T\bar{q}_2\right)\omega\right]. \quad (20)$$

Here, we claim that the proposed forward solver is applicable to the arbitrary tip shape, since the concept of the Green's function is used. A tip of the arbitrary shape has its own Green's function, which accounts from point-to-point electrostatic interaction for the working background that includes the tip, air gap, sample, substrate, and ground. We can easily see that our mathematical formula does not rely on special shape of tip, such as spheroid, cone-sphere, cylinder-sphere, and paraboloid. The Green's function for an arbitrary tip can be numerically calculated and then stored in the commercial software.

B. *Numerical Validation*

The calculated contrast capacitance via the proposed forward solver is compared with the commercial-software simulation result. As shown in Fig. 10(a), different homogeneous lossless materials are filled in the domain D_{in}, the relative permittivity ε_p of which varies from 1 to 40. The calculated result agrees well with the simulated one, and the discrepancy between two results is smaller than 1%. To illustrate the influence of the material conductivity σ, the

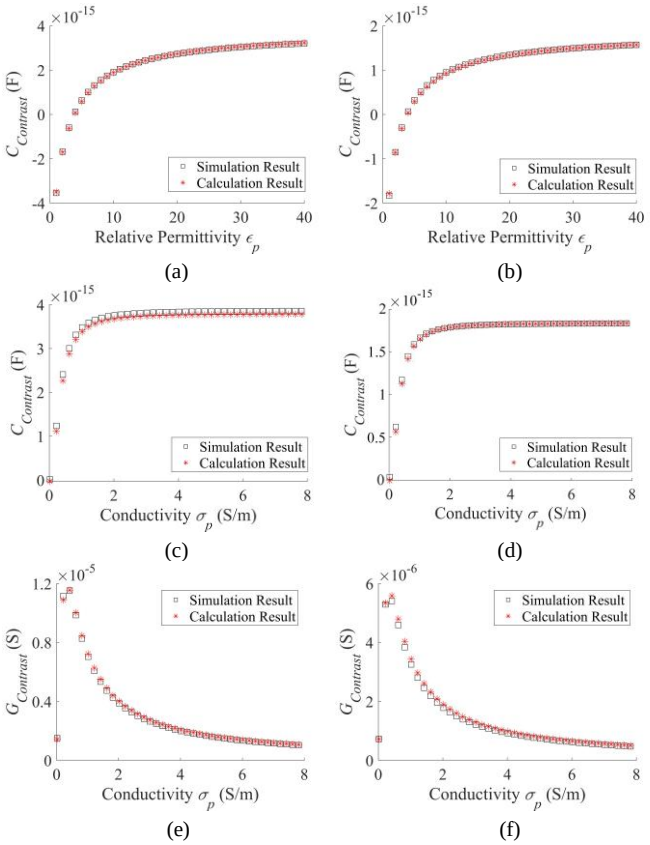

Fig. 10. The comparison between the calculated and simulated results of different tips. (a) Various relative permittivity and (c) various conductivity versus the contrast capacitance, and (e) various conductivity versus the contrast conductance of the cylinder-sphere tip. (b) Various relative permittivity and (d) various conductivity versus the contrast capacitance, and (f) various conductivity versus the contrast conductance of the cone-sphere tip.

effective region is filled by the lossy material with relative permittivity ε_p of 3.8 and conductivity σ_p varying from 0.02 S/m to 7.82 S/m. As shown in Fig. 10(c) and (e), the existence of the conductivity contributes to the contrast capacitance and the contrast conductance. The calculation result agrees well with the simulation result. Moreover, the comparison between the calculated C_{contrast} and $G_{contrast}$ and the simulated ones of the cone-sphere tip is also given in the Fig. 10(b), (d) and (f). The discrepancy between the simulation result and the calculation result of the cone-sphere tip is still small, which validates that the proposed forward solver is applicable to different tip shapes.

IV. Nonlinear Dielectric Characterization

In previous studies, a parameter fitting method is usually adopted in the dielectric characterization, which relies heavily on the established database. Based on the proposed forward solver, an iterative algorithm is proposed to characterize the relative permittivity of unknown samples from measured data via the CR-based NFSMM. To validate the performance of the proposed iterative algorithm, two unknown lossless samples are utilized in the measurement in this section.

A. *Inverse Formulation and Implementation*

Given the implementation convenience in the inverse

TABLE II

IMPLEMENTATION PROCEDURE OF DIELECTRIC CHARACTERIZATION

Algorithm: The inverse permittivity retrieval method

Input: ΔC_m: measured contrast signal, $\bar{M}_1, \bar{M}_2, \bar{M}_3, M_4$: calculated vector for the inverse procedure, ε_1: initial guess of the unknown relative permittivity, $F_{threshold}$: The threshold for stopping the iteration.

Output: ε_n: retrieved relative permittivity of the unknown sample.

For $n = 1,2,\ldots$ until $F_{ts}^n \le F_{threshold}$, do:

1 Calculate $\bar{\bar{D}}_{\varepsilon_n}$.

2 Calculate the gradient of the objective function g (λ=10^{-5}):

$$g = \frac{\partial F_{ts}}{\partial \varepsilon_p} = \sum_{ts=1}^{N} -2\left[\left(\bar{M}_1 + \bar{M}_3\right)\cdot \bar{\bar{D}}_{\varepsilon}^{-1} \cdot \frac{\partial \bar{\bar{D}}_{\varepsilon}}{\partial \varepsilon_p} \cdot \bar{\bar{D}}_{\varepsilon}^{-1} \cdot \bar{M}_2\right]^* \times \left(\Delta C_c - \Delta C_m\right) \Big/ \left\|\Delta C_m\right\|^2 + 2\lambda\varepsilon_p$$

where * is the conjugate operation.

3 Calculate the Polak–Ribière–Polyak direction:

If n=1, $\rho_1 = -g_1$.

Otherwise, $\rho_n = -g_n + \mathrm{Re}\left[\left(g_n - g_{n-1}\right)^* \cdot g_n\right] \Big/ \left\|g_{n-1}\right\|^2$

4 Calculate the search length following the Wolfe conditions:

For $m = 0,1,2,\ldots$ until

$F_{ts}(\varepsilon_{n-1}) - F_{ts}\left(\varepsilon_{n-1} + \gamma^m \rho_n\right) \ge -\delta\gamma^m g\left(\varepsilon_{n-1} + \gamma^m \rho_n\right)\rho_n$

($\gamma = 0.9$, 0<δ<1 is an adjusted parameter in optimization)

End For

5 Update relative permittivity $\varepsilon_n = \varepsilon_{n-1} + \gamma^m \rho_n$

End For

procedure, ε_p is firstly multiplied on both sides of (13)

$$\bar{\bar{\mathrm{D}}}_p \bar{\phi}_2 - \bar{\bar{\mathrm{G}}} \bar{q}_2 = 0 \tag{21}$$

where $\bar{\bar{\mathrm{D}}}_p$ becomes the only term related to ε_p. Then the rescaling process is made on (14) and (21) to avoid the severe ill condition in the inverse procedure [35]:

$$\bar{\bar{\mathrm{D}}}_t \bar{\phi}_2 - \bar{\bar{\mathrm{G}}}_t \bar{q}_{2t} = 0 \tag{22}$$

$$\bar{\bar{\mathrm{H}}} \bar{\phi}_2 - \bar{\bar{\mathrm{G}}}_{bt} \bar{q}_{2t} = \bar{\phi}_2^i \tag{23}$$

in which $\bar{\bar{\mathrm{D}}}_t = \bar{\bar{\mathrm{D}}}_p$, $\bar{\bar{\mathrm{G}}}_t = t_1 \bar{\bar{\mathrm{G}}}$, $\bar{\bar{\mathrm{G}}}_{bt} = t_1 \bar{\bar{\mathrm{G}}}_b$ and $\bar{q}_{2t} = \bar{q}_2 / t_1$ with t_1 being constant value (t_1=10^3 in this paper). Then the expression of the boundary potential is derived as

$$\bar{\phi}_2 = \bar{\bar{D}}_{\varepsilon}^{-1} \bar{\bar{\mathrm{G}}}_t \cdot \bar{\bar{\mathrm{G}}}_{bt}^{-1} \cdot \bar{\phi}_2^i, \tag{24}$$

where $\bar{\bar{D}}_{\varepsilon} = \bar{\bar{D}}_t + \bar{\bar{\mathrm{G}}}_t \cdot \bar{\bar{\mathrm{G}}}_{bt}^{-1} \cdot \bar{\bar{\mathrm{H}}}$. Therefore, the contrast signal can be calculated as follows:

$$\Delta C = -\bar{L}^T \bar{\phi}_2 - \bar{P}^T \bar{q}_2 = (\bar{M}_1 + \bar{M}_3)\bar{\bar{D}}_{\varepsilon}^{-1} \bar{M}_2 + M_4, \tag{25}$$

in which $\bar{M}_1 = -\bar{L}^T$, $\bar{M}_2 = \bar{\bar{\mathrm{G}}}_t \cdot \bar{\bar{\mathrm{G}}}_{bt}^{-1} \cdot \bar{\phi}_2^i$, $\bar{M}_3 = t_1 \bar{P}^T \cdot \bar{\bar{\mathrm{G}}}_{bt}^{-1} \cdot \bar{\bar{\mathrm{H}}}$ and $M_4 = -t_1 \bar{P}^T \cdot \bar{\bar{\mathrm{G}}}_{bt}^{-1} \cdot \bar{\phi}_2^i$. In (25), $\bar{\bar{D}}_{\varepsilon}$ is the only term related to the unknown permittivity ε_p. As a result, the proposed method could recast the dielectric characterization problem as a minimization of an objective function that is a normalized mismatch between the calculated contrast capacitance and the measured one:

$$Min: f_{ts}\left(\varepsilon_p\right) = \sum_{ts=1}^{N} \left\|\Delta C_c^{ts}\left(\varepsilon_p\right) - \Delta C_m^{ts}\right\|^2 \Big/ \left\|\Delta C_m^{ts}\right\|^2, \tag{26}$$

where the subscript *ts* denotes the index of tip-sample distances.

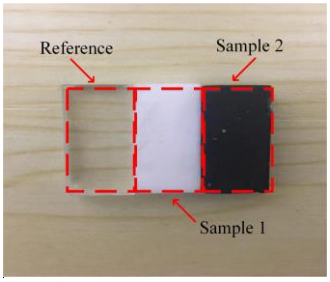

Fig. 11. The illustration of two investigated samples.

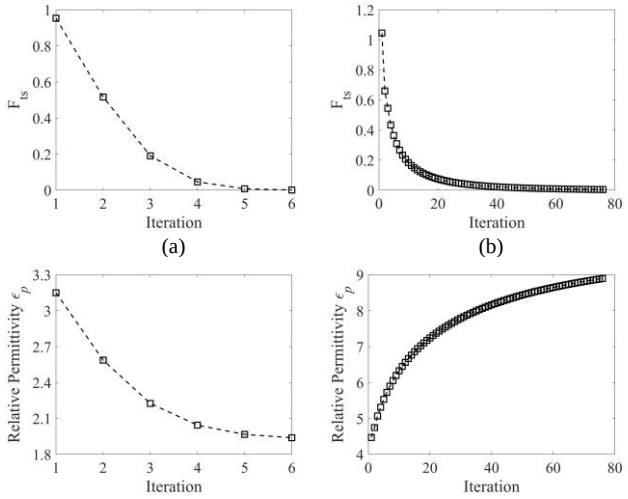

Fig. 12. The iteration procedure of the relative permittivity retrieval. (a) F_{ts} of Sample 1. (b) F_{ts} of Sample 2. (c) Retrieved ε_p of Sample 1. (d) Retrieved ε_p of Sample 2.

Due to the ill-posedness in the objective function, a Tikhonov regularization term is introduced in the objective function, and the new objective function is defined as:

$$Min: F_{ts}\left(\varepsilon_p\right) = \sum_{ts=1}^{N} \left\|\Delta C_c^{ts}\left(\varepsilon_p\right) - \Delta C_m^{ts}\right\|^2 \Big/ \left\|\Delta C_m^{ts}\right\|^2 + \lambda \left\|\varepsilon_p\right\|^2, \tag{27}$$

where λ is the regularization parameter and can be empirically determined. The conjugate gradient (CG) method is used to minimize the objective function (27), and the search length in the iteration is determined by the Wolfe conditions [36]. The whole implementation procedure is summarized in Table II.

B. *Experimental Validation*

To validate the performance of the proposed dielectric characterization method, two unknown samples are selected and measured by the NFSMM, the lateral dimension of which is 2.1 mm×1.2 mm. The thickness of the samples are around 5 mm, as illustrated in Fig. 11. The 5.1 mm homogeneous Quartz sample is selected as the reference sample in the calibration procedure. The operating frequency of the CR-based NFSMM is 1.41 GHz, and the tip aperture and tip sample distance is same as the parameters reported in Fig. 9. After measuring the reference sample, the tip is moved to the testing sample in the constant height mode, i.e., the absolute height of the tip is fixed during horizontal movement. Then, the tip moves vertically over the testing sample to meet 0.2 mm tip-sample distance. In order to improve the accuracy of the reconstruction result, the signal at 4 different positions are recorded for the inversion algorithm. According to the observation in Section II. B, the

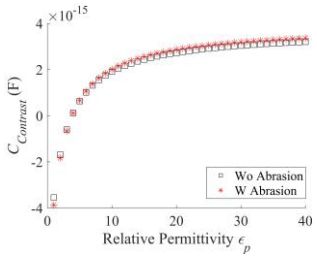

Fig. 13. The comparison between the tip with and without abrasion.

measurement of the unknown sample thickness could be simplified. The measured signals for the inverse algorithm are obtained and converted to the contrast capacitance via the obtained S'_{11} in calibration procedure. The iteration procedure for the dielectric characterization is illustrated in Fig. 12. Given the inevitable noise in the measurement data, $F_{threshold}$ in Table II is empirically selected as 0.5%. The retrieved permittivity ε_p for the first unknown sample is 1.94, while the measured permittivity ε_m via the transmission line method is 2.0. The relative error *Re*, calculated by $|\varepsilon_p - \varepsilon_m| \,/\, |\varepsilon_m|$, is 3.0%. The retrieved permittivity ε_p for the second unknown sample is 8.90, while the measured permittivity ε_m via the transmission line method is 9.0. The relative error *Re* is 1.1%.

To investigate the influence of the tip abrasion, the simulation result of the cylinder-sphere tip with 3 μm abrasion depth is illustrated in Fig. 13. The simulation condition is same as that in Section III. B. Due to the abrasion, a slight discrepancy occurs, and the maximum error is 8.5% occurring at ε_p = 1. In order to avoid such an influence, one more calibration procedure needs to be conducted after the measurement to check whether the abrasion occurs in the measurement. If the calibrated measurement result after the measurement matches well with that before the measurement, the abrasion will not be considered to occur. Otherwise, the measurement data will be inaccurate, and the experiment needs to be conducted again with a new tip.

V. Conclusion

In this paper, a systematic material characterization method via the CR-based NFSMM is proposed. A truncated model with the specific boundary conditions is not only applied to an arbitrary tip shape, but also reduces the time cost in simulation. The discrepancy between the simulated contrast capacitance and the measured result is less than 2.1% in calibration procedure.

Based on the distribution of the electric energy, the effective interaction region in the CR-based NFSMM is investigated. The determination of the effective region reduces the computation area of the tip-sample interaction to a small domain, which creates a condition to apply the Huygens' principle in the proposed forward solver for homogeneous sample investigation. Moreover, it is observed that the tip-sample interaction is more sensitive to the tip-sample distance rather than the thickness of the sample when the sample thickness is larger than 4 mm.

Based on the proposed forward solver, a nonlinear iteration algorithm is proposed for the dielectric characterization of the homogeneous sample. The relative error between the retrieved result and the measured result is less than 3%. Our work provides an easy and reliable pathway to quantitatively characterize the dielectric property of the homogeneous sample via the CR-based NFSMM, where the requirement on the sample dimension and the measurement environment has been reduced considerably. The extension of the proposed method to the micro- or nano-scale will be our future work, where the roughness of the surface and the tilt in the measurement will be taken into account.

References

[1] J. Baker-Jarvis, E. J. Vanzura, and W. A. Kissick, "Improved technique for determining complex permittivity with the transmission/reflection method," *IEEE Trans. Microw. Theory Techn.*, vol. 38, no. 8, pp. 1096–1103, 1990.

[2] E. Kilic, A. Yapar, and F. Akleman, "Complex permittivity determination of dielectric materials by waveguide measurements: A robust approach based on integral equations," *IEEE Microw. Wirel. Compon. Lett.*, vol. 21, no. 11, pp. 631–633, 2011.

[3] M. D. Janezic and J. Baker-Jarvis, "Full-wave analysis of a split-cylinder resonator for nondestructive permittivity measurements," *IEEE Trans. Microw. Theory Techn.*, vol. 47, no. 10, pp. 2014–2020, Oct. 1999.

[4] J. Krupka, "Measurements of the Surface Resistance and the Effective Conductivity of Copper Cladded Laminates Employing Dielectric Resonator Technique," *IEEE/MTT-S International Microwave Symposium*, Jun. 2007, pp. 515–518.

[5] K. Murata, A. Hanawa, and R. Nozaki, "Broadband complex permittivity measurement techniques of materials with thin configuration at microwave frequencies," *J. Appl. Phys.*, vol. 98, no. 8, p. 084107, 2005.

[6] F.-Y. Han, F.-H. Li, J.-Y. Liu, and P.-K. Liu, "Effective-medium characteristics of reflective metasurface: A quasi-one-port network theory," *IEEE Trans. Microw. Theory Techn.*, vol. 67, no. 8, pp. 3284–3296, 2019.

[7] C. A. Bryant and J. B. Gunn, "Noncontact Technique for the Local Measurement of Semiconductor Resistivity," *Rev. Sci. Instrum.*, vol. 36, no. 11, pp. 1614–1617, Nov. 1965.

[8] E. Ash and G. Nicholls, "Super-resolution aperture scanning microscope," *Nature*, vol. 237, no. 5357, pp. 510–512, 1972.

[9] M. Fee, S. Chu, and T. W. Hänsch, "Scanning electromagnetic transmission line microscope with sub-wavelength resolution," *Opt. Commun.*, vol. 69, no. 3, pp. 219–224, Jan. 1989.

[10] H. P. Huber *et al.*, "Calibrated nanoscale capacitance measurements using a scanning microwave microscope," *Rev. Sci. Instrum.*, vol. 81, no. 11, p. 113701, Nov. 2010.

[11] M. Farina, D. Mencarelli, A. Di Donato, G. Venanzoni, and A. Morini, "Calibration Protocol for Broadband Near-Field Microwave Microscopy," *IEEE Trans. Microw. Theory Techn.*, vol. 59, no. 10, pp. 2769–2776, Oct. 2011.

[12] M. Farina *et al.*, "Disentangling time in a near-field approach to scanning probe microscopy," *Nanoscale*, vol. 3, no. 9, pp. 3589–3593, 2011.

[13] M. Farina *et al.*, "Investigation of Fullerene Exposure of Breast Cancer Cells by Time-Gated Scanning Microwave Microscopy," *IEEE Trans. Microw. Theory Techn.*, vol. 64, no. 12, pp. 4823–4831, Dec. 2016.

[14] X. Jin *et al.*, "Imaging of exosomes by broadband scanning microwave microscopy," in *2016 46th European Microwave Conference (EuMC)*, Oct. 2016, pp. 1211–1214.

[15] C. Vlahacos, R. Black, S. Anlage, A. Amar, and F. Wellstood, "Near-field scanning microwave microscope with 100 μm resolution," *Appl. Phys. Lett.*, vol. 69, no. 21, pp. 3272–3274, 1996.

[16] C. Gao, T. Wei, F. Duewer, Y. Lu, and X.-D. Xiang, "High spatial resolution quantitative microwave impedance microscopy by a scanning tip microwave near-field microscope," *Appl. Phys. Lett.*, vol. 71, no. 13, pp. 1872–1874, 1997.

[17] M. Abu-Teir, M. Golosovsky, D. Davidov, A. Frenkel, and H. Goldberger, "Near-field scanning microwave probe based on a

dielectric resonator," *Rev. Sci. Instrum.*, vol. 72, no. 4, pp. 2073–2079, 2001.
[18] G. Gramse *et al.*, "Nondestructive imaging of atomically thin nanostructures buried in silicon," *Sci. Adv.*, vol. 3, no. 6, p. e1602586, 2017.
[19] M. C. Biagi *et al.*, "Nanoscale electric permittivity of single bacterial cells at gigahertz frequencies by scanning microwave microscopy," *ACS Nano*, vol. 10, no. 1, pp. 280–288, 2016.
[20] X. Wu *et al.*, "Quantitative measurements of nanoscale permittivity and conductivity using tuning-fork-based microwave impedance microscopy," *Rev. Sci. Instrum.*, vol. 89, no. 4, p. 043704, 2018.
[21] T. Wei, X. Xiang, W. Wallace-Freedman, and P. Schultz, "Scanning tip microwave near-field microscope," *Appl. Phys. Lett.*, vol. 68, no. 24, pp. 3506–3508, 1996.
[22] C. Gao and X.-D. Xiang, "Quantitative microwave near-field microscopy of dielectric properties," *Rev. Sci. Instrum.*, vol. 69, no. 11, pp. 3846–3851, 1998.
[23] J. Park, S. Hyun, A. Kim, T. Kim, and K. Char, "Observation of biological samples using a scanning microwave microscope," *Ultramicroscopy*, vol. 102, no. 2, pp. 101–106, Jan. 2005.
[24] S. Gu, K. Haddadi, A. El Fellahi, and T. Lasri, "Setting parameters influence on accuracy and stability of near-field scanning microwave microscopy platform," *IEEE Trans. Instrum. Meas.*, vol. 65, no. 4, pp. 890–897, 2016.
[25] R. W. P. King, "The electromagnetic field of a horizontal electric dipole in the presence of a three-layered region," *J. Appl. Phys.*, vol. 69, no. 12, pp. 7987–7995, 1991.
[26] A. N. Reznik, "Quasistatics and electrodynamics of near-field microwave microscope," *J. Appl. Phys.*, vol. 115, no. 8, p. 084501, 2014.
[27] K. Lai, W. Kundhikanjana, M. Kelly, and Z. Shen, "Modeling and characterization of a cantilever-based near-field scanning microwave impedance microscope," *Rev. Sci. Instrum.*, vol. 79, no. 6, p. 063703, 2008.
[28] Z. Wei, "Modeling and inversion in near-field microwave microscopy and electrical impedance tomography," Ph.D. dissertation, National University of Singapore, Singapore, 2016.
[29] Z. Wei *et al.*, "Quantitative Theory for Probe-Sample Interaction With Inhomogeneous Perturbation in Near-Field Scanning Microwave Microscopy," *IEEE Trans. Microw. Theory Techn.*, vol. 64, no. 5, pp. 1402–1408, May 2016.
[30] L. Ma, N. Leng, X. Z. Ye, M. Jin, and M. Bai, "The Distribution Measurement of the Photo-induced Plasma in Semiconductor by Near-field Scanning Microwave Microscopy," *Photonics & Electromagnetics Research Symposium - Fall (PIERS - Fall)*, Dec. 2019, pp. 169–172.
[31] Z. Wei and X. Chen, "Numerical study of resolution in near field microscopy for dielectric samples," in *2015 IEEE International Symposium on Antennas and Propagation & USNC/URSI National Radio Science Meeting*, Jul. 2015, pp. 910–911.
[32] W. C. Chew, *Waves and fields in inhomogeneous media*. New York: Van Nostrand Reinhold, 1990.
[33] X. Chen, *Computational methods for electromagnetic inverse scattering*. Singapore: Wiley, 2018.
[34] J. D. Jackson, *Classical electrodynamics*. New York : Wiley, 1999.
[35] Z. Wei, R. Chen, and X. Chen, "Nonlinear reconstruction of multilayer media in scanning microwave microscopy," *IEEE Trans. Instrum. Meas.*, vol. 68, no. 1, pp. 197–205, 2018.
[36] Y.-H. Dai and Y. Yuan, "A nonlinear conjugate gradient method with a strong global convergence property," *SIAM J. Optim.*, vol. 10, no. 1, pp. 177–182, 1999.

Yulong Zhou was born in Xi'an, China, in July 1993. He is currently pursuing a Ph.D. degree from the Department of Electrical and Computer Engineering, National University of Singapore, Singapore. His research interests include electromagnetic inverse scattering and directly applying it on non-destructive imaging.

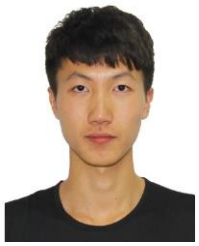

Ning Leng received his B.S. and M.S. degrees from Beihang University (BUAA), Beijing, China, in 2018 and 2021, respectively. He is currently pursuing the Ph.D. degree at the Microwave Engineering Lab., Beihang University. His research interests include near-field scanning microwave microscopy and permittivity measurement.

Zhun Wei is a tenure-track assistant professor at College of Information Science and Electronic Engineering, Zhejiang University. He was a Postdoctoral Fellow in Center for Advanced Imaging, Faculty of Arts and Sciences at Harvard University from 2019 to 2020 and also a Visiting Postdoc in Stanford University from 2018 to 2019. He received the B.S. degrees in University of Electronic Science and Technology of China, in 2012, and the Ph.D. degree in National University of Singapore, in 2016. He was a recipient of 2016 Best Student Paper Competition Award, IEEE Singapore MTT/AP Joint Chapter, and a recipient of "Ulrich L. Rohde Innovative Conference Paper Award" at ICCEM 2019. Dr. Wei is an Administrative Editor and Associate Editor of Progress In Electromagnetics Research (PIER) and also serves as Technical Program Co-chair and Session chair in several international conferences. Since 2016, Dr. Wei has published more than 40 peer-reviewed papers on topics of electromagnetic inverse problem, physics-assisted deep learning, uncertainty quantification, and inverse design.

Xiuzhu Ye joined Department of Information and Electronics, Beijing Institute of Technology (BIT) in May 2019, as Associate professor and PhD director. Before joining BIT, she worked as assistant professor at Beihang University. Before that she did her post-doc research in Department of Electrical and Computer Engineering, National University of Singapore (NUS), since May 2012. She received her Bachelor's Degree of Communication Engineering in Harbin Institute of Technology in 2008 and PhD degree in electrical engineering in NUS in 2012. Her current research interests include inverse problems, biomedical imaging system, security imaging systems, through wall imaging radar and related machine learning algorithms. She has published more than 80 scientific articles in the related areas, including 20+ papers in top journals. She is currently an IEEE senior member. She also serves as youth deputy director at EMC branch and member of council at Young Women Scientists Club in China Electronics Society.

Ming Bai received his B.Sc. and Ph.D. degrees from Physics Department of the University of Science and Technology of China (USTC) in 1996 and 2002, respectively. From 2002 to 2006, he worked as a Postdoctoral Researcher technology (LFSP), Spanish National Research Council (CSIC). He joined Beihang University (BUAA) China, in 2006. Currently he worked as a Professor in Microwave Engineering Lab., Beihang University. His research interests include computational electromagnetic and microwave imaging.

Xudong Chen (Fellow, IEEE) received the B.S. and M.S. degrees in electrical engineering from Zhejiang University, China, in 1999 and 2001, respectively, and the Ph.D. degree from the Massachusetts Institute of Technology, Cambridge, MA, USA, in 2005. Since 2005, he has been with the National University of Singapore, Singapore, where he is currently a Professor. He has published 160 journal papers on inverse scattering problems, material parameter retrieval, microscopy, and optical encryption. He has authored the book *Computational Methods for Electromagnetic Inverse Scattering* (Wiley-IEEE, 2018). His research interests include mainly electromagnetic wave theories and applications, with a focus on inverse problems and computational imaging. He is recently working on mm-wave imaging algorithms and solving inverse problems via machine learning. Dr. Chen was a recipient of the Young Scientist Award by the Union Radio Scientifique Internationale in 2010 and a recipient of the "Ulrich L. Rohde Innovative Conference Paper Award" at 2019 IEEE ICCEM conference. He was an Associate Editor of the *IEEE Transactions on Microwave Theory and Techniques* during 2015-2019 and has been an Associate Editor of the *IEEE Journal of Electromagnetics, RF and Microwave in Medicine and Biology* since 2020. He has been members of organizing committees of more than 10 conferences, serving as General Chair, TPC Chair, Award Committee Chair, etc. He was the Chair of IEEE Singapore MTT/AP Joint Chapter in 2018. He is a Fellow of Electromagnetics Academy.